

# 9

---

## HYDROGEN-BONDING IN ACETYLACETONE\*

### 9.1 Introduction

Hydrogen bonds are ubiquitous in chemistry and biology. While the strength of the “classical hydrogen bond” is around 3–5 kcal/mol, hydrogen bond strengths span more than two orders of magnitude (0.2–40 kcal/mol), with the nature of the hydrogen bond (HB) varying as a function of its electrostatic, dispersion, charge-transfer, and covalent contributions.<sup>1</sup> In the extreme limit, for symmetric hydrogen bonds X–H–X, the H-atom is equally

---

\* Adapted from Srinivasan, R.; Feenstra, J. S.; Park, S. T.; Xu, S. J.; Zewail, A. H., *J. Am. Chem. Soc.* **2004**, *126*, 2266; Xu, S. J.; Park, S. T.; Feenstra, J. S.; Srinivasan, R.; Zewail, A. H., *J. Phys. Chem. A* **2004**, *108*, 6650.

shared; no distinction can then be made between the donor and acceptor, or the “covalent” X–H and “noncovalent” H···X bond.<sup>2</sup> Such unusually strong interactions can result either from charge-transfer assisted HBs in polarizable systems or from so-called resonance-assisted<sup>†</sup> HBs due to conjugation in neutral systems.<sup>3-5</sup>

Enolones, the enol tautomers of  $\beta$ -diketones, contain two neutral donor and acceptor oxygen atoms connected by a system of conjugated double bonds (Scheme 9–1); the consequent synergistic reinforcement of H-bonding and  $\pi$ -delocalization can lead to strong intramolecular resonance-assisted O–H···O HBs. Increasing delocalization may transform the HB from an asymmetric O–H···O interaction (double well) to a symmetric O–H–O bond (single well), with the O···O distance being a measure of the strength of the HB. In the limit of complete delocalization, the C–C and C=C bonds as well as the C–O and C=O bonds become equal to each other, the O···O distance becomes very short, and the H-atom lies midway between the two oxygens. Acetylacetonone (AcAc), a prototypical enolone, has been the subject of numerous

---

<sup>†</sup> Strictly speaking, resonance involves the superposition of two or more structures with different electronic distributions but *identical* nuclear positions. Here, besides single- and double-bond electronic conjugation, motion of the hydrogen atom is also involved.

experimental<sup>6-18</sup> and theoretical efforts<sup>19-25</sup> to understand the nature of such strong HBs.

AcAc comprises two tautomeric forms in dynamic equilibrium, with the enol form dominating in the gas phase at room temperature due to stabilization by the internal HB (Scheme 9–2).<sup>13, 19</sup> Previous gas-phase electron diffraction experiments present conflicting enol structures: Lowrey *et al.*<sup>6</sup> and Andreassen and Bauer<sup>7</sup> report a symmetric ( $C_{2v}$ ) structure with a symmetric, linear HB, while Iijima *et al.*<sup>8</sup> support an asymmetric ( $C_s$ ) structure with an asymmetric, bent HB. Surprisingly, the two experiments reporting a symmetric structure give very different O···O distances, (2.381 Å<sup>6</sup> *vs.* 2.514 Å<sup>7</sup>). Moreover, theoretical investigations remain unsettled on the relative energies of these structures,<sup>21</sup> placing  $C_{2v}$  anywhere from slightly below<sup>19</sup> to >20 kcal/mol above<sup>23</sup> the  $C_s$  structure.

In this chapter we elucidate the keto–enol tautomeric equilibrium, the structure of both keto and enol forms, and the nature of the intramolecular O–H···O HB in enolic AcAc using electron diffraction—thereby resolving this long-standing controversy in the literature. With its proven ability to study complex molecular systems in thermal equilibrium, our third-generation Ultrafast Electron Diffraction apparatus (UED-3) was employed to study the gas-phase diffraction of ground-state AcAc (2,4-pentanedione, 99+%, Aldrich) at 155°C.

## 9.2 Experimental

The molecular sample was introduced into the chamber through a nozzle maintained at 155 °C. Acetylacetone (2,4-pentanedione) was purchased from Aldrich (>99.0%) and degassed before use by three cycles of the freeze–pump–thaw procedure.

The starting geometries for structural analysis were obtained by quantum chemical (DFT) calculations at the B3LYP/6-311G(d,p) level. Structural refinement was conducted with Monte Carlo sampling and least-squares fitting incorporated into home-built analysis software. Theoretical models were quantitatively rated by their R values, a typical statistical measure used in electron diffraction.

## 9.3 Ground State

Figure 9–1 shows the ground-state diffraction image of the H-transfer reaction and Fig. 9–2 shows the modified molecular scattering intensity,  $sM(s)$ , and its sine Fourier transform, the radial distribution curve  $f(r)$ , whose peaks reflect the relative density of internuclear distances in the molecule.<sup>26</sup> The first peak at  $\sim 1.5$  Å corresponds to direct bond distances in both the enol and keto forms, the peak at  $\sim 2.5$  Å to second nearest-neighbor distances, and

the peaks at longer distances to the unique O $\cdots$ O and C $\cdots$ O distances in the enol and keto tautomers.

Structural determination of AcAc tautomers requires an accurate estimate of the relative populations of the enol and keto forms. Diffraction data were fit using a mixture of enol ( $C_s$ ) and keto AcAc, with their starting geometries derived from density functional theory (DFT) calculations. Initial fitting of the populations of these DFT structures yielded an enol–keto ratio of  $88:12 \pm 1$ , which is in stark contrast to that expected at  $155^\circ\text{C}$ —thermodynamic equilibrium constants obtained by a variety of techniques (NMR, UV, IR)<sup>12-16</sup> predict a ratio between 71:29 and 79:21 in the gas phase. To resolve this discrepancy, we revisited the starting geometry of the keto form, which is free to undergo internal rotation about its C–C single bonds.<sup>19, 20</sup> The resultant array of keto rotamers was accounted for by floating the skeletal (and methyl) torsion angles of the DFT keto structure. The partially-refined keto structure is quite different from that reported in the literature—the oxygen atoms are much further apart ( $\sim 3.520 \text{ \AA}$ ; dihedral  $\angle\text{OCCO} = 104.7^\circ$ ) compared to that previously reported ( $\sim 2.767 \text{ \AA}$ ; dihedral  $\angle\text{OCCO} = 48.6^\circ$ ).<sup>6</sup>

Refitting the equilibrium population using this partially-refined keto structure gave  $78:22 \pm 4$ , in excellent agreement with the results of gas-phase NMR<sup>13</sup> and IR absorption,<sup>16</sup> thus highlighting the crucial importance of keto

internal rotation. It is pertinent to note here that simple calculations of equilibrium populations from DFT energies (using a fixed keto conformation) predict a ratio of  $\sim 98:2$  at  $155^\circ\text{C}$  due to a serious underestimation of the entropic term ( $2.4 \text{ cal/mol/K}$ ); using the experimental<sup>13-15</sup> value of  $8.3 \text{ cal/mol/K}$ , we in fact obtain a ratio of  $\sim 80:20$ . Furthermore, using a  $C_{2v}$  enolic model underestimates the ratio at  $68:32 \pm 3$ .

Structural refinement of the enol was then performed using the fit values for the equilibrium ratio and the keto geometry. Figure 9–2 shows the remarkable agreement between experiment and theory. The refined enolic structure is asymmetric, with all direct bond distances and angles being within  $\sim 0.02 \text{ \AA}$  and  $\sim 3^\circ$  of the DFT values, respectively (Fig. 9–3). Differences between the carbon–carbon distances ( $0.084 \text{ \AA}$ ) and carbon–oxygen distances ( $0.059 \text{ \AA}$ ) are far greater than the corresponding standard deviations and clearly distinguish between single and double bonds—a manifestation of structural asymmetry. The  $\text{O}\cdots\text{O}$  distance of  $\sim 2.592 \text{ \AA}$  in this structure is longer than those previously reported by electron diffraction at room temperature ( $2.512 \text{ \AA}$ <sup>8</sup>) and X-ray crystallography ( $2.535 \text{ \AA}$ <sup>10</sup> and  $2.547 \text{ \AA}$ <sup>11</sup>). These studies, along with neutron scattering in crystals,<sup>9</sup> liquid-phase NMR<sup>18</sup> and gas-phase vibrational spectroscopy,<sup>17</sup> are consistent with an asymmetric structure. Due to the relatively weak scattering of the hydrogen atom, in our fit, the  $\text{O-H}$ ,  $\text{H}\cdots\text{O}$  distances and the  $\text{O-H}\cdots\text{O}$  angle were held at DFT values

(1.003 Å, 1.683 Å, and 148.4°, respectively). In light of the insensitivity of electron diffraction to hydrogen, it is surprising that Iijima *et al.*<sup>8</sup> report a significantly out-of-plane H-atom ( $\angle\text{HOCC}=26^\circ$ ), which, though in reasonable agreement with a then-available crystal structure,<sup>10</sup> manifests as unusually large error bars (0.016 Å) in their fit O–H distance. A more recent x-ray crystal structure<sup>11</sup> supports the H-atom to be nearly in the molecular plane;  $\angle\text{HOCC} \sim 4^\circ$ .

The diffraction results reported here shed new light on the nature of the hydrogen bond in resonant and tautomeric structures. The keto structure with its large internal rotation exhibits a rotation-averaged dihedral angle of  $\sim 105^\circ$  between the carbonyls at the reported temperature. The enolic structure clearly indicates that AcAc does exhibit some  $\pi$ -delocalization leading to shorter C–C, C–O and longer C=C, C=O bonds compared to ‘unperturbed’ distances in enols.<sup>3-5</sup> However, this delocalization is not strong enough to give a symmetric skeletal geometry. The resulting long O $\cdots$ O distance is significant in making the homonuclear O–H $\cdots$ O hydrogen bond localized and asymmetric.

The dynamics of hydrogen motion (O–H $\cdots$ O) involves not only the O $\cdots$ O coordinate but also changes in skeletal geometry. In a symmetric double-well picture with ‘left’ and ‘right’ structures, there are two ( $\pm$ ) states (symmetric and anti-symmetric), and the probability of finding the structure

in either is 50%, independent of the interaction. The time scale for hydrogen motion depends on the total internal energy and the height of the barrier, which in turn depends on the O $\cdots$ O separation—for short enough values, the structure becomes that of a single well. On the ultrashort timescale, the potential is asymmetric.<sup>22, 27</sup> It would be interesting to resolve the dynamics in real time using the new developments of UED on this and higher energy structures.

#### 9.4 Structural Dynamics

In reactions involving conjugated hydrogen-bonded structures, the effects of electron delocalization and resonance can lead to multiple pathways that are determined by the nature of the initial structure(s) involved. While the nature of the ground-state structure is now resolved, less is known about the excited states and their reactions. The ultraviolet spectrum of vapor phase AcAc shows a broad structureless absorption that peaks at  $\sim 266$  nm and is assigned to the first  $\pi\pi^*$  transition ( $S_2$  state) of the enol tautomer.<sup>14, 28</sup> The photochemistry has been studied spectroscopically in matrices,<sup>29-31</sup> solutions,<sup>32</sup> and in the gas phase.<sup>33-35</sup> Whereas spectroscopic techniques rely on selectivity to monitor state dynamics, UED resolves the ultrafast structural dynamics of the reaction, as demonstrated earlier for thermal, fragmentation, and ring opening reactions.

The possible reaction pathways of isolated, gas-phase AcAc upon 266 nm excitation are shown in Scheme 9–3.

We elucidated the dominance of the OH-loss pathway, the structure of the resulting OH elimination product, and the relevant timescale.

## 9.5 Results and Discussion

Two dimensional time-resolved diffraction frames were collected for a range of time delays from  $-77$  to  $+1273$  ps with respect to the arrival of the initiating laser pulse. Frames recorded at each time point were converted to the modified molecular scattering curves,  $sM(s)$ , for electron diffraction structural analysis. The radial distribution curves,  $f(r)$ , were obtained by Fourier transform of the  $sM(s)$  curves. Frames obtained before time-zero contain information only on the ground-state structure of AcAc. For the time-resolved diffraction analysis, the ground-state data before time-zero was used as a reference and differenced from post-time-zero data to create difference curves,  $\Delta sM(s)$  and  $\Delta f(r)$ , thereby obtaining the net structural change from reactants to products.<sup>26</sup> Figure 9–4 shows the time-resolved difference radial distribution curves using  $-77$  ps as the reference. The curves clearly map out the reaction—the time-dependent depletion of old bonds and formation of new bonds.

In order to reveal the reaction pathway(s), the experimental  $\Delta sM(s)$  and  $\Delta f(r)$  curves at the +1273 ps delay (reference = -77 ps) are compared with theoretical  $\Delta sM(s)$  and  $\Delta f(r)$  curves of several reaction channels: isomerization, Norrish cleavage, and elimination, as shown in Fig. 9-5. This visual comparison provides an intuitive way of choosing an appropriate starting point for structural refinement. Although some isomerization of the chelated (H-bond intact) enol into non-chelated enol in matrices<sup>29-31</sup> and in solution<sup>32</sup> has been studied, the poor match ( $R = 1.103$ ) between this model and the data (see Fig. 9-5) indicates that the pathway is not significant in the isolated reaction; the experimental  $\Delta f(r)$  shows high-amplitude peaks corresponding to bond scission that are not provided by the theoretical model. Norrish Type-I reactions, such as the loss of the acetyl or methyl groups were considered and discarded as poor models for the data (see Fig. 9-5). This is consistent with the structural dynamics discussed below.

The tautomerization channel, i.e., formation of keto and enol tautomers after internal conversion to the “hot” ground-state, also studied by spectroscopy in matrices,<sup>30</sup> appeared to fit the data ( $R = 0.508$ ; not shown) when utilizing quantum chemically determined structures. A mixture of the structures of both keto and enol tautomers in their ground states at 2256 K

was used.<sup>‡</sup> AcAc with this internal energy will consist of enol and keto tautomers in a 1:2 ratio. Structural refinement for this channel did not greatly improve the quality of the fit. Moreover, fitting the fractions of keto and enol tautomers eliminated the enol contribution completely, in contradiction to the thermodynamics of population distribution.

Superior structural refinement results were obtained with the use of the OH loss model ( $R = 0.533$ , see Fig. 9–5). OH loss has been observed by laser-induced fluorescence (LIF) spectroscopy of gas-phase AcAc.<sup>33-35</sup> In our UED study, combinations of the previously mentioned channels were tested by comparing the data with mixtures of several theoretical models. This produced slightly improved fits (as more degrees of freedom are present). However, since the OH loss channel always remained the dominant component, structural refinement was carried out with this channel being the reaction pathway.

Having identified the reaction channel, the structure of its corresponding product, the 3-penten-2-on-4-yl radical, was then refined as shown in Fig. 9–6. The final refined structure is shown in Fig. 9–7 ( $R =$

---

<sup>‡</sup> This temperature was calculated considering a statistical distribution of the absorbed energy of a single photon among all modes in the ground state.

0.338). The refined covalent bond distances and angles show some deviations from the equilibrium structures predicted by quantum chemical calculations. The bonds connecting the methyl groups to the remainder of the carbon skeleton,  $r(\text{C1-C2})$  and  $r(\text{C4-C5})$ , are longer by 0.080 and 0.045 Å, respectively. Also at variance from theory, the acetyl group is rotated out of the plane of the molecule by  $\sim 20^\circ$  instead of being coplanar. This indicates that the radical is able to rotate around the C–C single bond. The fitted value reflects an average over all the rotations present in the products.

Structurally, due to the loss of intramolecular hydrogen bonding, the resonance of the conjugated system is disrupted, and the bonds revert to a more unperturbed state. The skeletal distances in the ground state enol,  $r(\text{C2-C3}) = 1.359$  Å,  $r(\text{C3-C4}) = 1.443$  Å, and  $r(\text{C4-O4}) = 1.262$  Å,<sup>36</sup> become  $1.304 \pm 0.025$  Å,  $1.482 \pm 0.023$  Å, and  $1.202 \pm 0.017$  Å, respectively, in the product radical where the hydrogen bond is severed and resonance stabilization is lost. Mean amplitudes of vibration were deduced to be consistent with a somewhat cold structure in agreement with a previous finding<sup>35</sup> that a significant fraction of internal energy is released into translational motion of the fragments (note that our initial thermal energy is higher than the temperature of the supersonic expansion<sup>35</sup>).

Using the refined product structure shown in Fig. 9–7, its fractional contribution to each of the other time points was obtained. The plot of the

product fraction versus time is shown in Fig. 9–8. Over the entire time scale, a time constant of  $247 \pm 34$  ps was obtained from nonlinear fitting using a first-order reaction model. In order to test the validity of a direct first order reaction (without intermediates), new diffraction-difference data were obtained by using a frame after time-zero as the reference. This alternative difference data (referred to hereafter as  $\Delta\Delta sM(s)$  or difference-difference data) are shown in Fig. 9–9 for the +1273 ps frame with the +73 ps frame as the reference. In a first order reaction, the resulting data would be lower in amplitude yet still correspond to the parent→product reaction scheme. Conversely, if the reaction has multiple steps, the entire parent contribution will be removed in the difference-difference data. This data will then contain information on the intermediate→product reaction. The data shown in Fig. 9–9 suggests the latter case and the presence of an intermediate structure.

Elimination of OH from the  $T_1$  ( $\pi\pi^*$ ) state of AcAc has been suggested in the literature.<sup>35</sup> The possibility of the  $T_1$  structure as the intermediate is tested by comparing theoretical  $\Delta\Delta sM(s)$  and  $\Delta\Delta f(r)$  with experimental data (see Fig. 9–9). The  $T_1$  state possesses a non-planar structure with the C–O moiety twisted  $66^\circ$  out of the skeletal plane resulting in internuclear distances drastically different from  $S_0$ ; for example, the O··O separation is 3.426 Å for the  $T_1$  structure, compared to 2.592 Å for the  $S_0$  structure.<sup>36</sup> The  $T_1$  structure does not fit the experimental  $\Delta\Delta sM(s)$  as the intermediate, ruling

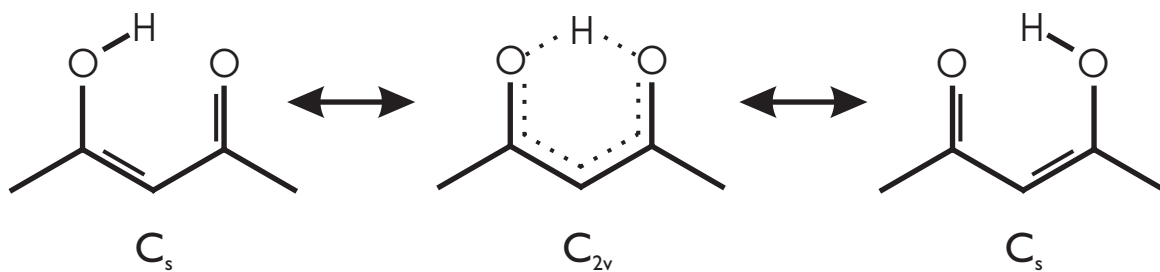
out a slow dissociation from  $T_1$  as the rate determining step of the reaction. Figure 9–9 suggests that the intermediate structure is of singlet character, manifested as a combination of  $S_1$  and  $S_2$  structures because of their proximity in energy.<sup>37</sup> Furthermore, the structureless absorption band<sup>14, 28, 34</sup> and absence of fluorescence<sup>33, 35</sup> suggest that the  $S_2$  state is very short-lived. Consequently, the observed rise is the rate determining step, the intersystem crossing (ISC) from  $S_1$  to  $T_1$ ; this long lifetime of  $S_1$  has also been observed for malonaldehyde.<sup>38</sup> The appearance of pseudo-first order behavior is consistent with ISC as the rate-determining step for the overall elimination reaction.

Structural dynamics can now be related to the reaction pathway(s) involving different electronic states. The transition from  $S_2$  to  $S_1$  is ultrafast (fluorescence was not observed<sup>33, 35</sup>), as discussed above. In the  $S_1$  ( $n\pi^*$ ) state, the structure is planar and the lifetime of molecules in this state is determined by the ISC to the  $T_1$  ( $\pi\pi^*$ ) state. The structure in the  $T_1$  state is non-planar (C–O moiety twisted  $66^\circ$  out of the skeletal plane), and as such, it promotes the cleavage of the OH radical in order to reform the double bond present in the final radical. It is now easy to understand why the dominant reaction channel is not a Norrish-type cleavage as would be prompted by a  $T_1$  structure of  $n\pi^*$  excitation. The structures involved in the dynamics of this elimination are pictured in Fig. 9–10. Figure 9–11 confirms that the observed

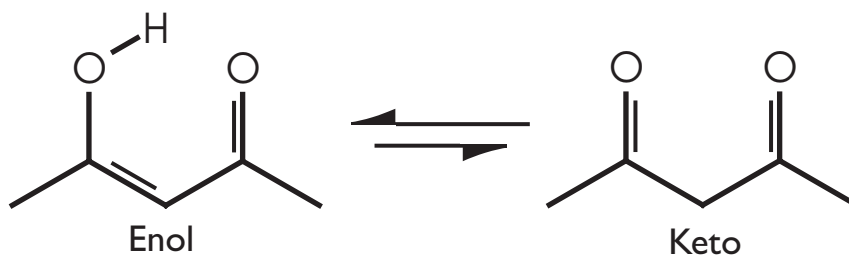
structural dynamics is not due to multi-photon processes but rather is the result of a one-photon process.

## 9.6 Conclusions

The sensitivity of UED to all nuclear positions reveals that the ground state of AcAc is of  $C_s$  asymmetric structure. The OH loss is the dominant channel after 266 nm excitation, but transient structures are found to precede the final product. The overall time constant for OH formation is determined to be  $247 \pm 34$  ps. The influence of resonance stabilization on the molecular structure of the ground state is lost in the  $T_1$  state, and the OH moiety is no longer co-planar with the conjugated bonds, aiding in efficient OH elimination. The  $\pi\pi^*$  nature of this structure facilitates reaction pathways that are not typical among ketones—OH-elimination from the  $\beta$  carbon as opposed to a Norrish Type-I cleavage. The absence of resonance stabilization results in the more “electron-localized” structure of the 3-penten-2-on-4-yl radical, and the change in bond distances is directly observed. With ultrafast electron diffraction it was possible to map out changes of structures with time on the energy/state landscape of the reaction.



**Scheme 9-1.** Structures of enolic acetylacetone.



**Scheme 9-2.** Enol-keto tautomerization by hydrogen shift.



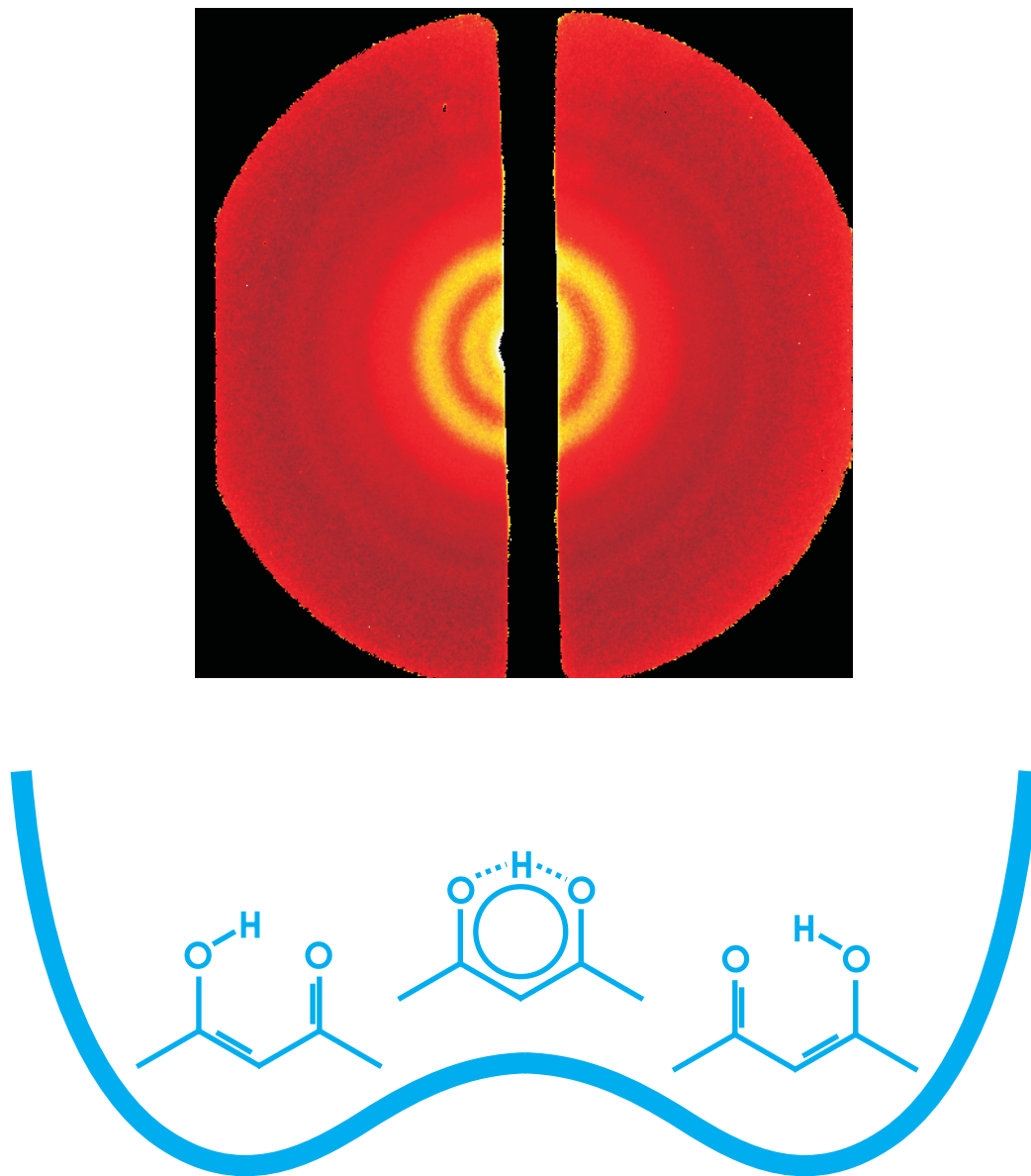


**Figure 9-1.** 2D ground-state diffraction image of acetylacetonone. Also shown schematically is the symmetric potential for the hydrogen motion between the two oxygen atoms in enolic acetylacetonone.

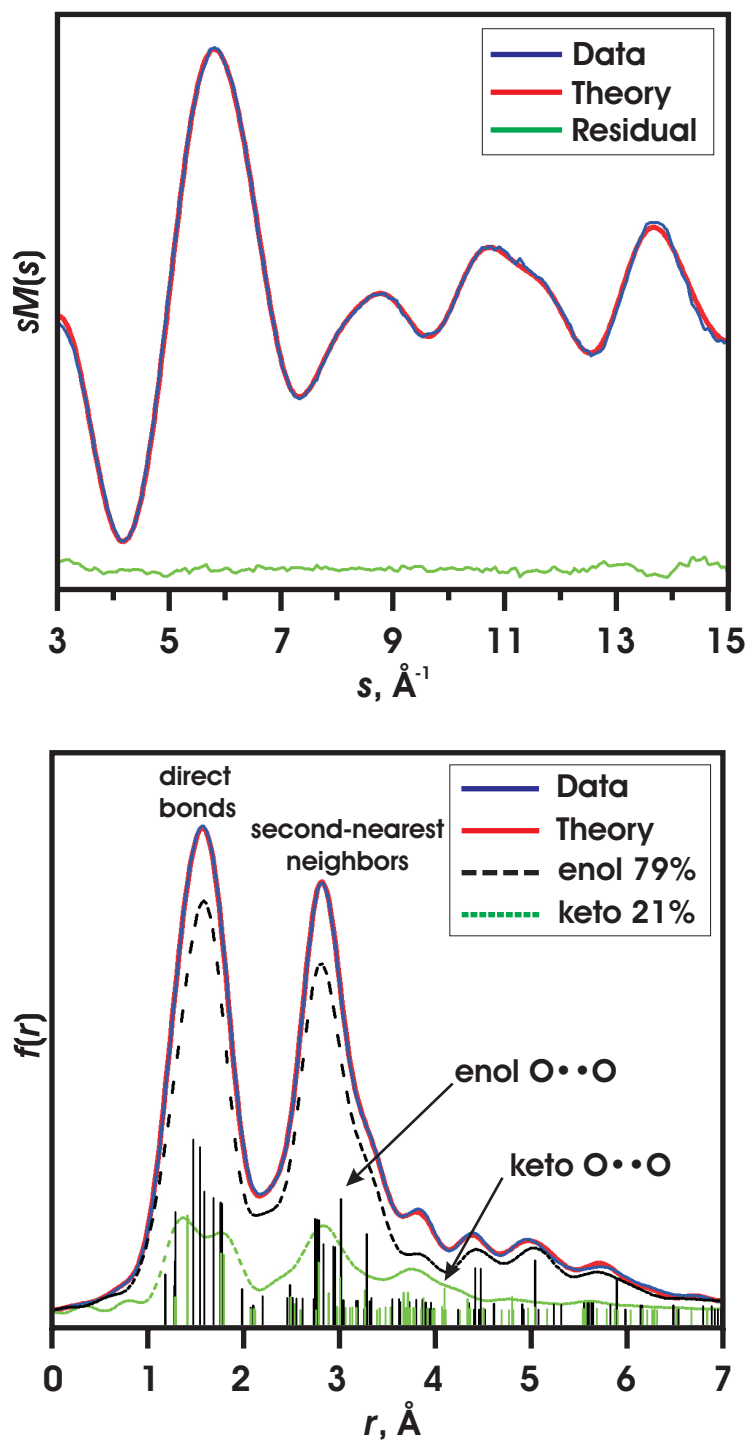
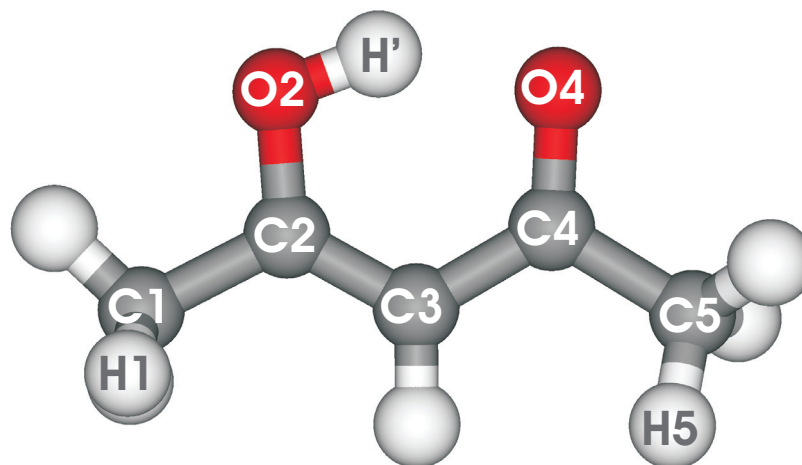


**Figure 9-2.** Diffraction data and structural refinement of acetylacetonone. (Top) Modified molecular scattering intensity,  $sM(s)$ . (Bottom) Total and species radial distribution curves,  $f(r)$ .



Distances	Angles
$r(\text{C1-C2}) = 1.504 \pm 0.021$ (1.495)	$\alpha(\text{C1-C2-C3}) = 123.6 \pm 1.1$ (124.1)
$r(\text{C2-C3}) = 1.359 \pm 0.034$ (1.370)	$\alpha(\text{C2-C3-C4}) = 120.4 \pm 1.0$ (120.4)
$r(\text{C3-C4}) = 1.443 \pm 0.019$ (1.444)	$\alpha(\text{C3-C4-C5}) = 118.2 \pm 1.0$ (118.6)
$r(\text{C4-C5}) = 1.518 \pm 0.023$ (1.513)	$\alpha(\text{C1-C2-O2}) = 112.9 \pm 2.7$ (113.7)
$r(\text{C2-O2}) = 1.321 \pm 0.021$ (1.325)	$\alpha(\text{C5-C4-O4}) = 118.7 \pm 3.1$ (119.7)
$r(\text{C4-O4}) = 1.262 \pm 0.005$ (1.244)	$\phi(\text{H1C1-C2C3}) = -57.2 \pm 16.5$ (-0.1)
	$\phi(\text{H5C5-C4C3}) = -19.3 \pm 4.8$ (-63.2)

**Figure 9-3.** Final refined structure of the enol tautomer of acetylacetone. Distances are in ångströms and angles are in degrees.

## Structural Dynamics

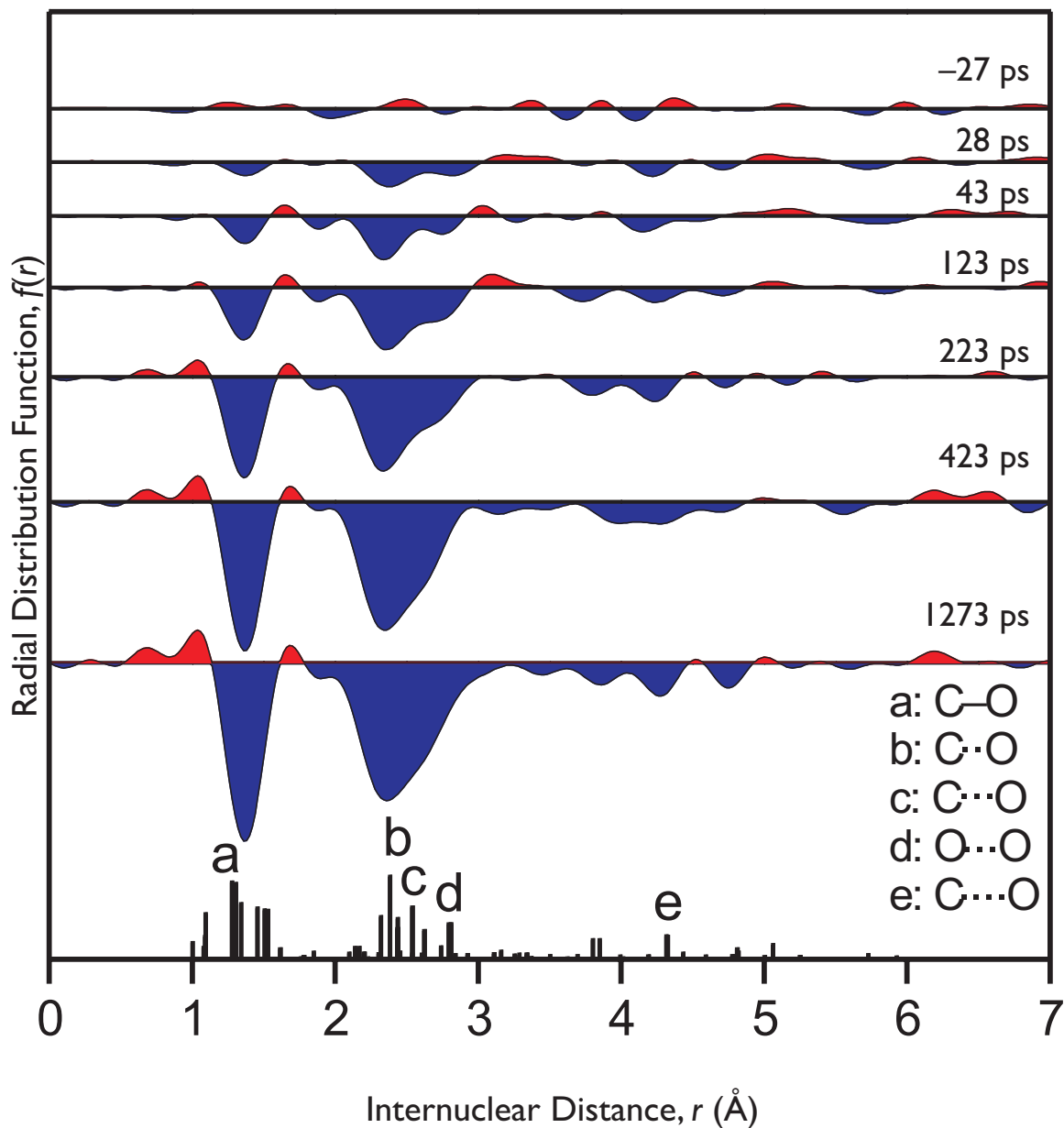


**Figure 9-4.** Observed structural dynamics of acetylacetonone. Shown are the time-resolved radial distribution curves,  $\Delta f(r;t)$ . The blue highlighted regions represent net depletion of internuclear pairs (“old bonds”). Red highlighting represents the formation of new distances. The vertical lines at the bottom indicate their relative contributions, proportional to  $nZ_iZ_j/r_{ij}$ .  $Z$  is the atomic number and  $r$  is the internuclear distance. Distances are in ångströms and angles are in degrees.

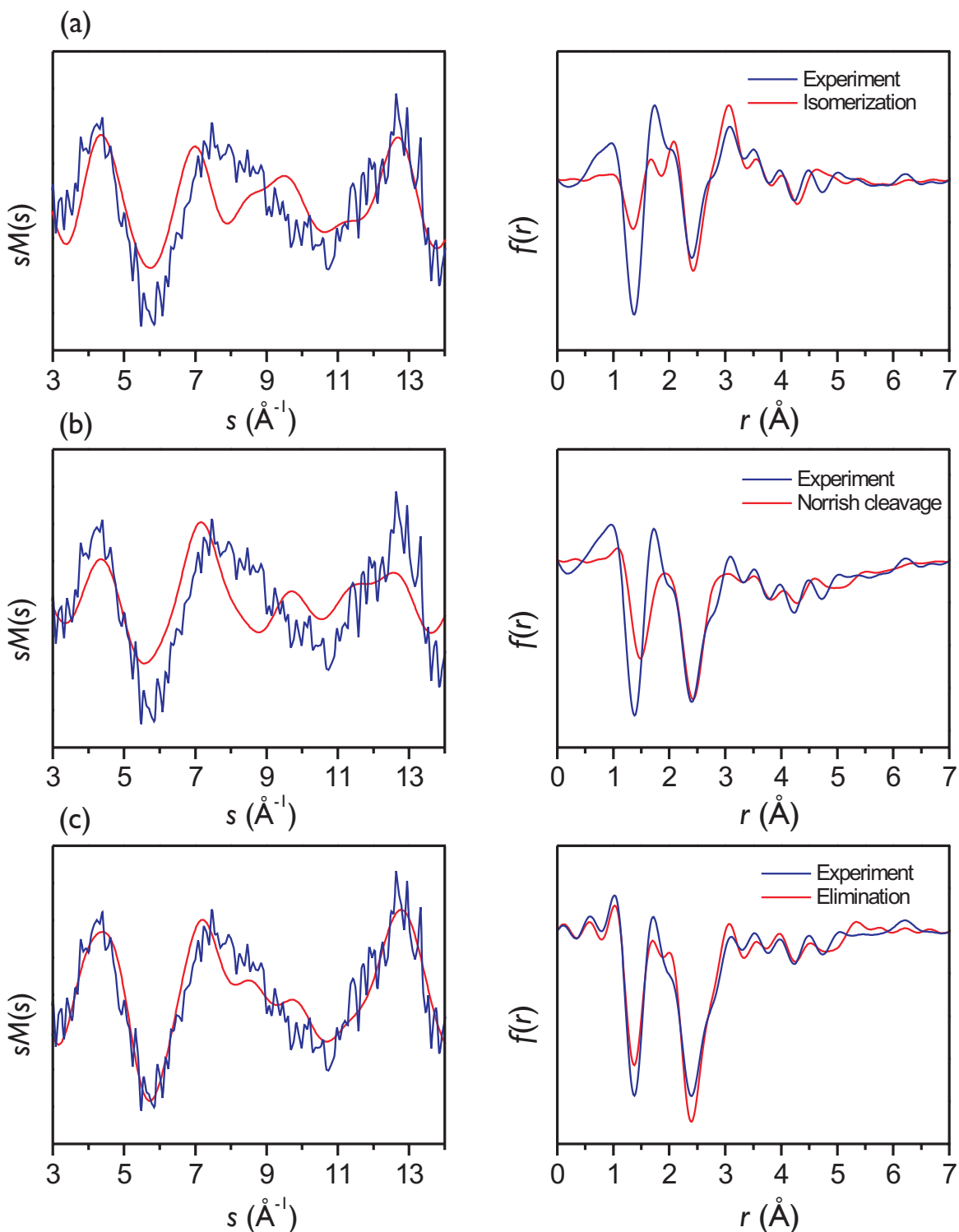


**Figure 9-5.** Experimental and theoretical diffraction-difference data ( $\Delta sM(s)$  and  $\Delta f(r)$ ); +1273 ps (reference = -77 ps) for different pathways. (a) Isomerization to *cis-trans-cis* enol.  $R = 1.103$ . (b) Norrish Type-I cleavage of the methyl group.  $R = 1.222$ . (c) Loss of the OH radical.  $R = 0.533$ . The minor difference in appearance of the experimental data is an effect of different background curves.

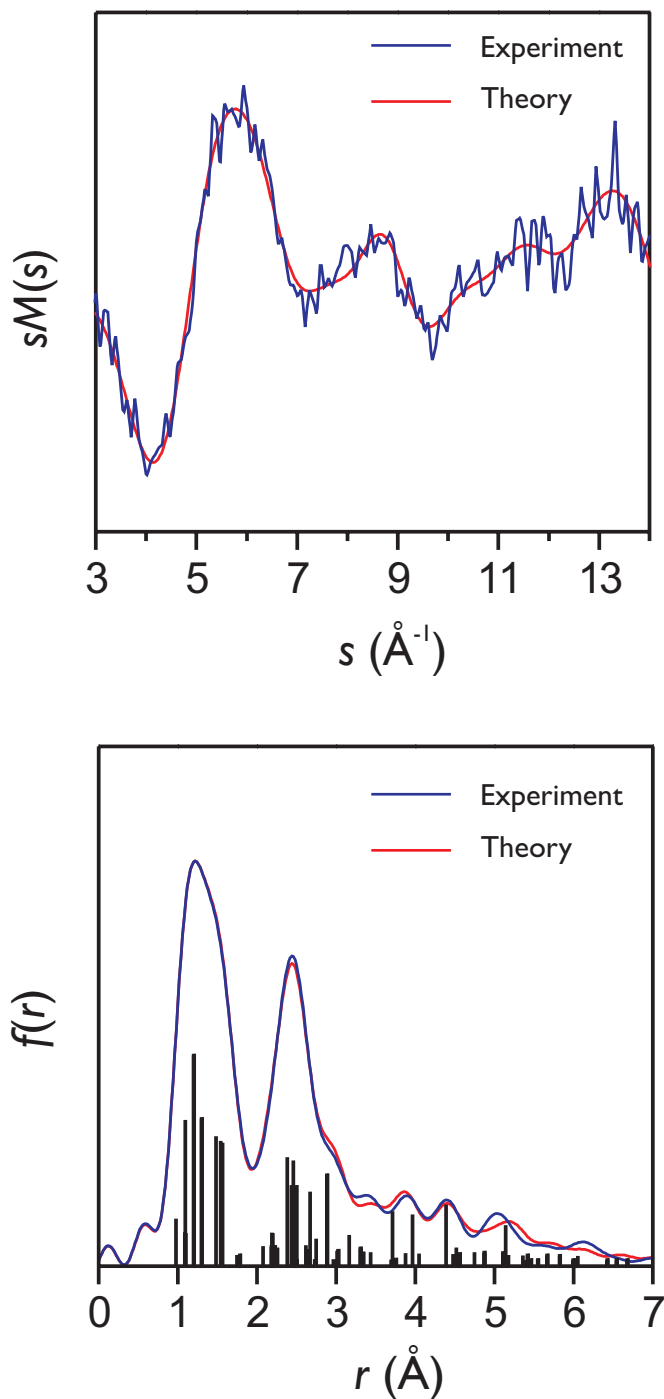
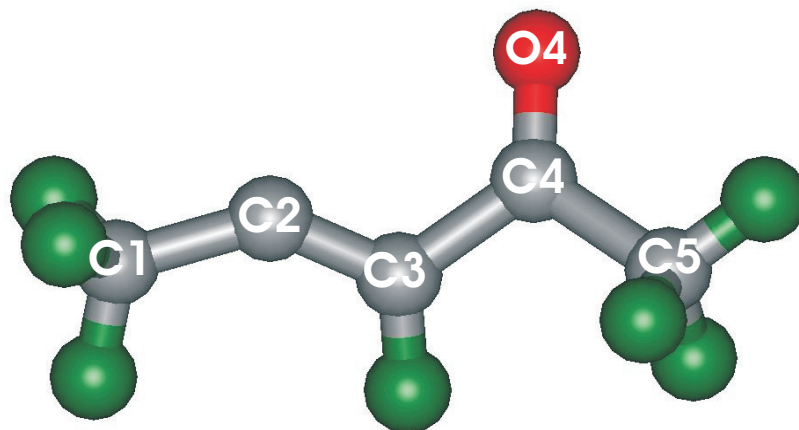


**Figure 9-6.** The refined theoretical  $sM(s)$  and  $f(r)$  curves and the +1273 ps “product only” data.  $R = 0.273$ . The bars below  $f(r)$  show the intensity contributed by each internuclear separation in the molecule, proportional to  $nZ_iZ_j/r_{ij}$ . In “product-only” format the fitted parent contribution to the reaction is added to the difference data leaving only the product signal.

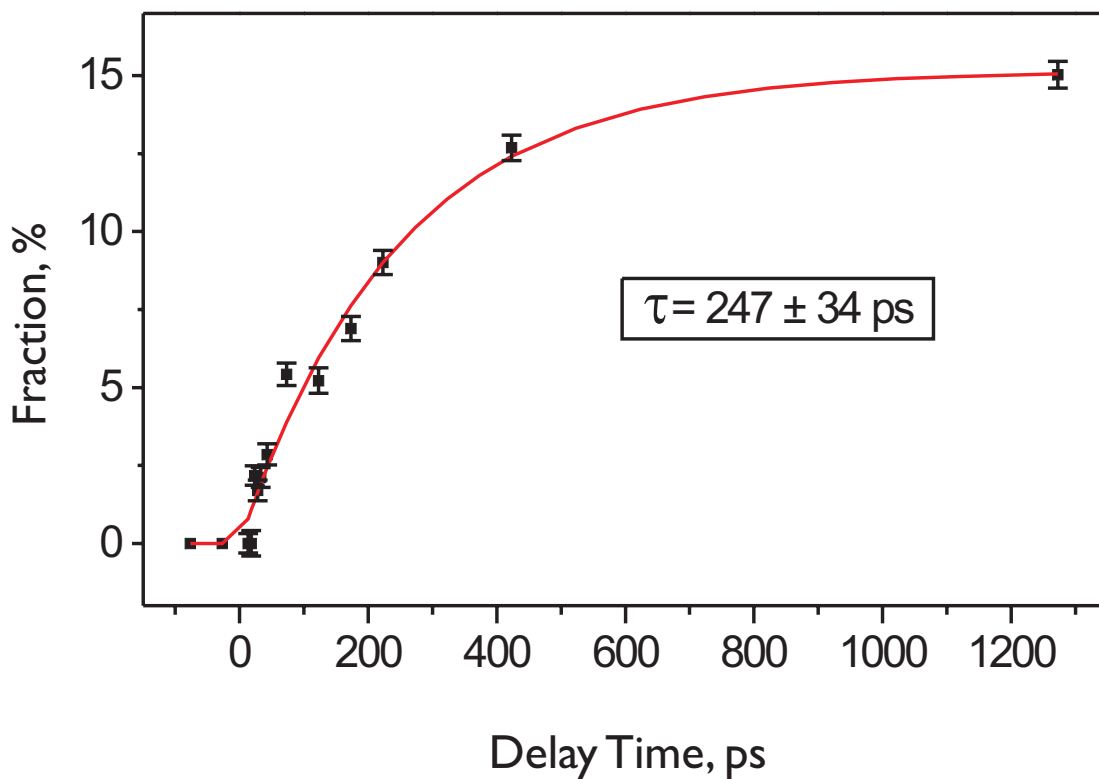


Distances		
	<i>experiment</i>	<i>DFT</i>
$r_1(\text{C1-C2})$	$1.542 \pm 0.023$	1.462
$r_2(\text{C2-C3})$	$1.304 \pm 0.025$	1.316
$r_3(\text{C3-C4})$	$1.482 \pm 0.023$	1.499
$r_4(\text{C4-C5})$	$1.564 \pm 0.047$	1.519
$r_5(\text{C4-O4})$	$1.202 \pm 0.017$	1.212

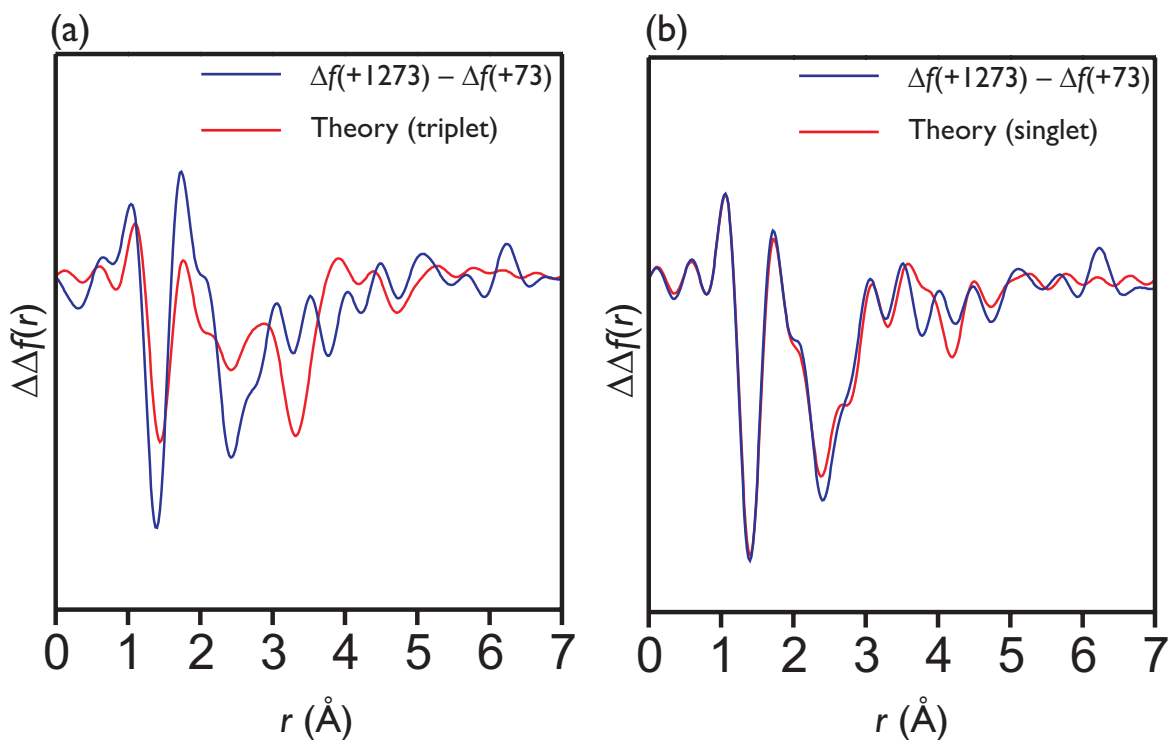
  

Angles		
	<i>experiment</i>	<i>DFT</i>
$\angle_1(\text{C1-C2-C3})$	$139.4 \pm 5.9$	141.5
$\angle_2(\text{C2-C3-C4})$	$121.8 \pm 1.7$	123.8
$\angle_3(\text{C3-C4-C5})$	$110.3 \pm 2.8$	115.4
$\angle(\text{C2C3-C4C5})$	$-159.8 \pm 14.2$	180

**Figure 9-7.** The refined structure of the 2-penten-4-on-3-yl radical. Also shown are the refined parameters of the fitted structure compared with starting values obtained by DFT. Distances are in ångströms and angles are in degrees.



**Figure 9-8.** Fraction of OH loss products for all experimental time slices, showing a rise time of  $247 \pm 34$  ps.



**Figure 9-9.** Difference-difference data. (a) +1273 ps frame–reference frame (+73 ps), and the theoretical model corresponding to  $T_1(\text{DFT}) \rightarrow \text{OH}$  loss products. (b) +1273 ps frame–reference frame (+73 ps), and the theoretical model corresponding to  $S \rightarrow \text{OH}$  loss products. S is an approximation of the singlet manifold structure made using a combination of  $S_1$  and  $S_2$  geometries (CASSCF) in  $\sim 1:3$  ratio (see text).

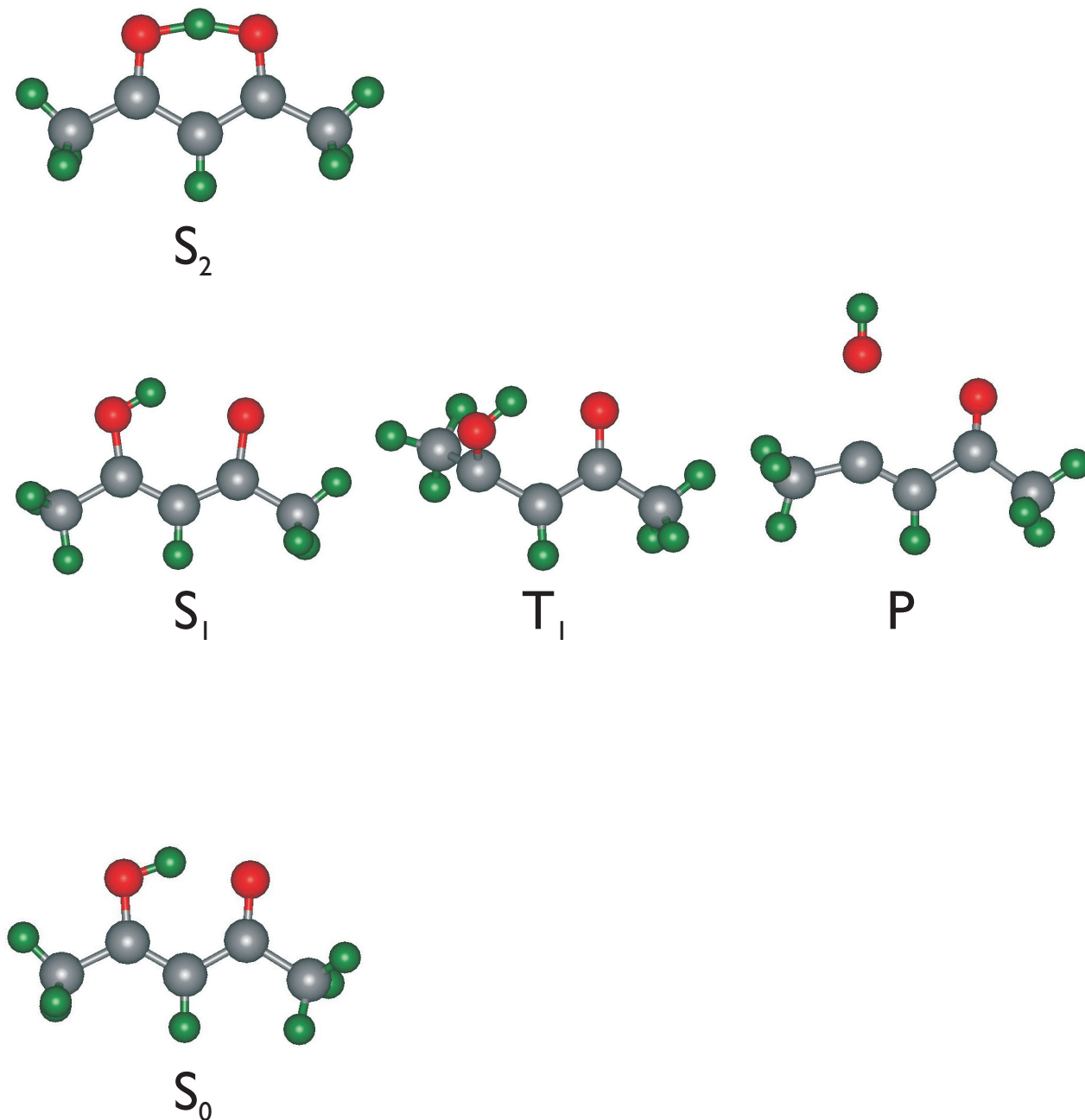


**Figure 9-10.** Structures involved in the dynamics of the OH elimination reaction. Ground-state ( $S_0$ ) and OH elimination product (P) structures were experimentally obtained using UED (see text). Excited state structures ( $S_1$ ,  $S_2$ ,  $T_1$ ) were obtained by *ab initio* methods at the CASSCF(10,9)/6-31G(d,p) level.

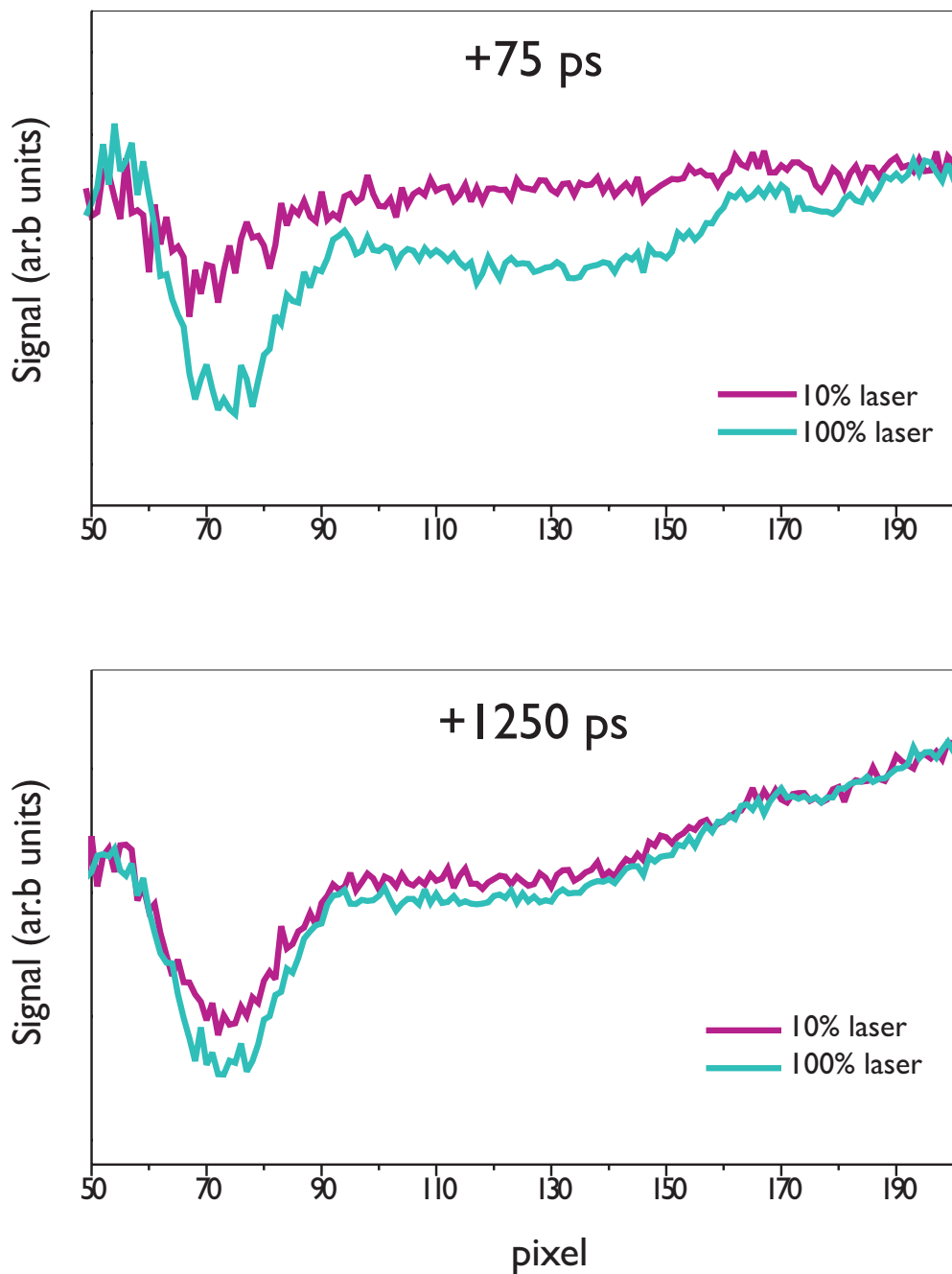


**Figure 9-11.** Power-dependence studies of UED observation of acetylaceton photochemistry. The comparison of the diffraction-difference signal at the two time slices indicates that the photochemistry is unaffected, except for an expected enhancement in the amplitude of the difference signal due to greater fractional change.

---

**References**

1. Steiner, T., *Angew. Chem.* **2002**, *41*, 48.
2. Perrin, C. L.; Nielson, J. B., *Annu. Rev. Phys. Chem.* **1997**, *48*, 511.
3. Gilli, G.; Bellucci, F.; Ferretti, V.; Bertolasi, V., *J. Am. Chem. Soc.* **1989**, *111*, 1023.
4. Gilli, P.; Bertolasi, V.; Ferretti, V.; Gilli, G., *J. Am. Chem. Soc.* **1994**, *116*, 909.
5. Gilli, P.; Bertolasi, V.; Pretto, L.; Ferretti, V.; Gilli, G., *J. Am. Chem. Soc.* **2004**, *126*, 3845.
6. Lowrey, A. H.; George, C.; D'Antonio, P.; Karle, J., *J. Am. Chem. Soc.* **1971**, *93*, 6399.
7. Andreassen, A. L.; Bauer, S. H., *J. Mol. Struct.* **1972**, *12*, 381.
8. Iijima, K.; Ohnogi, A.; Shibata, S., *J. Mol. Struct.* **1987**, *156*, 111.
9. Johnson, M. R.; Jones, N. H.; Geis, A.; Horsewill, A. J.; Trommsdorff, H. P., *J. Chem. Phys.* **2002**, *116*, 5694.
10. Camerman, A.; Mastropaolo, D.; Camerman, N., *J. Am. Chem. Soc.* **1983**, *105*, 1584.
11. Boese, R.; Antipin, M. Y.; Blaser, D.; Lyssenko, K. A., *J. Phys. Chem. B* **1998**, *102*, 8654.
12. Harris, R. K.; Rao, R. C., *Org. Magn. Reson.* **1983**, *21*, 580.

13. Folkendt, M. M.; Weiss-Lopez, B. E.; Chauvel Jr., J. P.; True, N. S., *J. Phys. Chem.* **1985**, *89*, 3347.
14. Nakanishi, H.; Morita, H.; Nagakura, S., *Bull. Chem. Soc. Jpn.* **1977**, *50*, 2255.
15. Hush, N. S.; Livett, M. K.; Peel, J. B.; Willett, G. D., *Aust. J. Chem.* **1987**, *40*, 599.
16. Powling, J.; Bernstein, H. J., *J. Am. Chem. Soc.* **1951**, *73*, 4353.
17. Tayyari, S. F.; Zeegers-Huyskens, T.; Wood, J. L., *Spectrochimica Acta* **1979**, *35A*, 1289.
18. Egan, W.; Gunnarsson, G.; Bull, T. E.; Forsen, S., *J. Am. Chem. Soc.* **1977**, *99*, 4568.
19. Dannenberg, J. J.; Rios, R., *J. Phys. Chem.* **1994**, *98*, 6714.
20. Ishida, T.; Hirata, F.; Kato, S., *J. Chem. Phys.* **1999**, *110*, 3938.
21. Bauer, S. H.; Wilcox, C. F., *Chem. Phys. Lett.* **1997**, *279*, 122.
22. Sharafeddin, O. A.; Hinsien, K.; Carrington, T.; Roux, B., *J. Comput. Chem.* **1997**, *18*, 1760.
23. Mavri, J.; Grdadolnik, J., *J. Phys. Chem. A* **2001**, *105*, 2039.
24. Grabowski, S. J., *J. Phys. Org. Chem.* **2003**, *16*, 797.
25. Delchev, V. B.; Mikosch, H.; St. Nikolov, G., *Monatsh. Chem.* **2001**, *132*, 339.

- 
26. Srinivasan, R.; Lobastov, V. A.; Ruan, C. Y.; Zewail, A. H., *Helv. Chim. Acta* **2003**, *86*, 1763.
27. Ando, K.; Hynes, J. T., *J. Phys. Chem. B* **1997**, *101*, 10464.
28. Walzl, K. N.; Xavier Jr., I. M.; Kuppermann, A., *J. Chem. Phys.* **1987**, *86*, 6701.
29. Roubin, P.; Chiavassa, T.; Verlaque, P.; Pizzala, L.; Bodot, H., *Chem. Phys. Lett.* **1990**, *175*, 655.
30. Nagashima, N.; Kudoh, S.; Takayanagi, M.; Nakata, M., *J. Phys. Chem. A* **2001**, *105*, 10832.
31. Coussan, S.; Manca, C.; Ferro, Y.; Roubin, P., *Chem. Phys. Lett.* **2003**, *370*, 118.
32. Veierov, D.; Bercovici, T.; Fischer, E.; Mazur, Y.; Yogev, A., *J. Am. Chem. Soc.* **1977**, *99*, 2723.
33. Yoon, M.-C.; Choi, Y. S.; Kim, S. K., *J. Chem. Phys.* **1999**, *110*, 11850.
34. Yoon, M.-C.; Choi, Y. S.; Kim, S. K., *Chem. Phys. Lett.* **1999**, *300*, 207.
35. Upadhyaya, H. P.; Kumar, A.; Naik, P. D., *J. Chem. Phys.* **2003**, *118*, 2590.
36. Srinivasan, R.; Feenstra, J. S.; Park, S. T.; Xu, S. J.; Zewail, A. H., *J. Am. Chem. Soc.* **2004**, *126*, 2266.
37. Lim, E. C., *J. Phys. Chem.* **1986**, *90*, 6770.

- 
38. Arias, A. A.; Wasserman, T. A. W.; Vaccaro, P. H., *J. Chem. Phys.* **1997**, *107*, 5617.